



Boosting oxygen reduction activity of Fe-N-C by partial copper substitution to iron in Al-air batteries

Jingsha Li^{a,1}, Jiajie Chen^{a,1}, Hao Wan^a, Jin Xiao^b, Yougen Tang^a, Min Liu^c, Haiyan Wang^{a,b,*}

^a Hunan Provincial Key Laboratory of Chemical Power Sources, College of Chemistry and Chemical Engineering, Central South University, Changsha, 410083, PR China

^b Department of Chemical and Biological Engineering, The Hong Kong University of Science and Technology, Clear Water Bay, Kowloon, Hong Kong, PR China

^c School of Physics and Electronics, Central South University, Changsha, 410083, PR China



ARTICLE INFO

Keywords:

Non-precious metal electrocatalyst
Cytochrome c oxidase
Al-air batteries
Oxygen reduction reaction
Density functional theory calculations

ABSTRACT

Iron and nitrogen co-doped carbon materials (Fe-N-C) have been widely investigated as one of the most promising electrocatalysts with low cost and excellent catalytic activity towards oxygen reduction reaction (ORR). Herein, inspired by the cytochrome c oxidase (CcO), we have proposed a high-performance bimetal Cu/Fe-regulating nitrogen-doped carbon (Cu-Fe-N-C) electrocatalyst via using partial copper substitution to iron in Fe-N-C. The optimized Cu-Fe-N-C composite displays much better catalytic activity than the pristine Fe-N-C indicated by 20 mV positive shift of onset potential (0.967 V vs RHE), 25 mV positive shift of half-wave potential (0.864 V vs RHE) and higher limiting-current density. The significantly enhanced performance is also manifested by a higher discharging cell voltage and better stability in practical Al-air batteries at a constant current density. Both experimental and computational results confirm that the significantly enhanced performance should be mainly ascribed to the synergistic effects of the bimetallic doping in Cu-Fe-N-C catalysts.

1. Introduction

Faced with the depletion of fossil fuels and corresponding energy crisis problem, fuel cells [1–3] and metal-air batteries [4–6] have been considered as the promising energy storage systems because of their high theoretical specific energy density. Among them, Al-air batteries with practical energy density up to 600 Wh Kg⁻¹ have become a hot research topic [7]. In the 1970s, Al-air batteries were mainly used for lighting mines, television broadcasts, navigation lights and so on [8]. In 2013, the electric vehicle powered by Al-air batteries has gone more than 1600 km. Despite these important progresses, their commercial applications are still impeded by the sluggish kinetics of oxygen reduction reaction (ORR) at cathodes. Currently, Pt-based materials have been still as the state-of-the-art catalysts towards ORR [9–11] as to catalytic activity and stability. Nevertheless, there are still many problems for these materials, such as low abundance, high cost, fuel crossover issue, and sensitivity to poisoning, which hinder their further application [12]. Consequently, developing novel non-precious metal catalysts (NPMCs) with excellent catalytic activity and stability towards ORR has become a mainstream, covering heteroatom-doped carbon materials (i.e. nitrogen, phosphorous and sulfur) [13–17], transition-

metal oxides and carbon hybrids [18–24], metal-organic macrocycles [25,26] and metal-nitrogen-carbon (M-N-C) [7,10,27–32]. Among them, Fe-N-C has received extensive attention because of the facile synthesis method and low cost. Traditional strategies to boost Fe-N-C include modifying carbon supports, optimizing synthesis conditions and nitrogen precursors [33–36]. In spite of some important progresses, further improvements toward the property of Fe-N-C is still necessary.

Enzymes have shown high activity and selectivity for certain reactions [37]. For instance, in the nature, cytochrome c oxidase (CcO) exists in the final step of respiration to facilitate the ORR process without releasing poisonous incompletely reduced oxygen species (PROS). Concerning the study of CcO, great efforts have been put on the coordination atmosphere of the Fe ion, multicopper complexes, and iron phthalocyanines [37–41]. Under physiological conditions, copper in CcO is considered as a redox site to help electron flux during the ORR process, thus prohibiting the formation of PROS and enhancing the oxygen-binding affinity and the selectivity of CcO [37]. However, till now, less attention has been paid to the possible cooperativity of Cu and Fe in improving the activity of Fe-N-C. Robert et al. [42] pioneered the preparation of a novel Cu-Fe/C catalyst, which exhibited similar catalytic activity with Pt/C even at a 6-fold lower loading. Recently, Masaru

* Corresponding author at: Hunan Provincial Key Laboratory of Chemical Power Sources, College of Chemistry and Chemical Engineering, Central South University, Changsha, 410083, PR China.

E-mail address: wanghy419@csu.edu.cn (H. Wang).

¹ These authors contributed equally to this work.

et al. [43] reported the Cu-Fe-N-C hybrid by using 3,5-diamino-1,2,4-triazole as copper complex, chloro (protoporphyrinato) iron(III) and oxidized Vulcan XC-72 as raw materials. In both approaches, expensive Fe/Cu complexes were involved. More importantly, possible synergistic effect between Cu and Fe sites remains unclear.

In this work, we use inexpensive CuCl, $\text{FeCl}_2 \cdot 4\text{H}_2\text{O}$, 1,10-phenanthroline and melamine as precursors to synthesize bimetallic Cu/Fe and nitrogen co-doped carbon materials for ORR in Al-air batteries. Based on the optimum synthesized conditions of Fe-N-C, the partial iron was replaced with copper to further enhance the ORR catalytic performance. The obtained Cu-Fe-N-C hybrid possesses the best catalytic activity when the Cu/Fe mole ratio in the precursor is 1:1. The optimum Cu-Fe-N-C hybrid consists of worm-like carbon nanotubes, bamboo-like carbon nanotubes, and graphene-like carbon nanosheets, which is distinctly different from those of Fe-N-C and Cu-N-C. The hybrid exhibits much better catalytic activity than Fe-N-C evidenced by a 25 mV positive shift of half-wave potential (0.864 V vs RHE). The significantly enhanced performance is also manifested by a higher discharging cell voltage and better stability in practical Al-air batteries. The density function theory (DFT) computation further verifies that the enhanced activity of Cu-Fe-N-C could be attributed to synergistic effect of Fe and Cu co-doping.

2. Experimental sections

2.1. Synthesis of Cu-FeN-C catalyst

Cu-Fe-N-C samples were synthesized by a facile pyrolysis. Firstly, 0.1 mmol of $\text{FeCl}_2 \cdot 4\text{H}_2\text{O}$ and CuCl- $\text{4H}_2\text{O}$ were dissolved into 30 mL of ethanol and followed by the slow addition of another solution with 2 mmol 1,10-phenanthroline solution and 30 mL ethanol under stirring for 30 min. Then 10 g of melamine was added into the above solution. With sonication for 30 min, the mixture was kept at 40 °C under stirring until the solvent was evaporated. The red powder was transferred to the porcelain boat and sintered at 900 °C for 1 h under Ar/H₂ to obtain Cu-Fe-N-C. Finally, Cu-Fe-N-C was etched in 0.5 M H₂SO₄ at 80 °C for 12 h to get rid of unstable nanoparticles (marked as Cu-Fe-N-C-acid). For comparison, Fe-N-C and Cu-N-C were also synthesized via the similar procedure without adding CuCl- $\text{4H}_2\text{O}$ and $\text{FeCl}_2 \cdot 4\text{H}_2\text{O}$, respectively. Furthermore, the influence of Fe-N-C with the molar ratio of $\text{FeCl}_2 \cdot 4\text{H}_2\text{O}$ and 1,10-phenanthroline was also studied.

2.2. Physical characterizations

X-ray diffraction (XRD) patterns were performed on a Bruker Corporation X-ray diffractometer (SIMENS D500) at 8° min⁻¹. The morphologies were characterized by scanning electron microscopy (Nova NanoSEM 230) and transmission electron microscope (FEI Titan G2 60-300 TEM). X-ray photoelectron spectroscopy (XPS) data were recorded on a K-Alpha1063 spectrometer. The Brunauer-Emmett-Teller (BET) surface areas were calculated according to N₂ adsorption isotherm (V-Sorb 2800 P). Before measuring, all samples were degassed at 150 °C for 3 h under vacuum.

2.3. Electrochemical tests

The ORR catalytic activity was evaluated by cyclic voltammetry (CV) and linear sweep voltammetry (LSV) curves on an electrochemical work station (CHI760 e) with a three-electrode system, in which Pt wire and saturated calomel electrode (SCE) were used as counter and reference electrode, respectively, and a glass carbon electrode loaded by catalyst ink as working electrode. The catalyst ink was prepared in the following: 6 mg of catalyst was dispersed in 950 μL ethanol with ultrasonication for 30 min and followed by another sonication after adding Nafion (50 μL, 5 wt %). Then 10 μL of catalyst ink was dripped onto a glassy carbon electrode (5.61 mm) and dried under infrared lamp

to obtain the working electrode. All potentials initially measured versus SCE were normalized to reversible hydrogen electrode (RHE) according to the Nernst equation $E(\text{RHE}) = E(\text{SCE}) + 0.0591 \times \text{pH} + 0.24$ [44].

To study the ORR mechanism, LSV curves were scanned cathodically at 10 mV s⁻¹ with various rotating speeds from 400 to 1600 rpm in O₂-saturated 0.1 M KOH. Koutecky-Levich (K-L) plots were used to calculate electron transfer number (*n*):

$$\frac{1}{J} = \frac{1}{J_L} + \frac{1}{J_K} = \frac{1}{B\omega^{1/2}} + \frac{1}{J_K} \quad (1)$$

$$B = 0.62nFC_0D_0^{2/3}\nu^{-1/6} \quad (2)$$

Where *J*, *J_L* and *J_K* are the experimentally measured current density, diffusion-limiting current density and kinetic current density, respectively. Here, ω represents the rotating speed (rpm), *F* is the Faraday constant, *C₀* and *D₀* are the bulk concentration and diffusion coefficient of O₂, respectively, and *v* is the kinetic viscosity.

Rotating ring-disk electrode (RRDE) measurements were also performed and the ring current was collected when fixing ring potential at 1.5 V vs RHE. The % HO₂⁻ and *n* were calculated according to the equations:

$$\% \text{HO}_2^- = 200 \times \frac{I_r/N}{I_d + I_r/N} \quad (3)$$

$$n = 4 \times \frac{I_d}{I_d + I_r/N} \quad (4)$$

Where *N* is the current collection efficiency of the Pt ring (0.37), *I_d* and *I_r* represent the disk and ring current, respectively.

2.4. The assembly of Al-air full cell

To analyze the performance in Al-air batteries, the discharging curves at constant current density were conducted on a Neware battery testing system at room temperature. 6 M NaOH containing 0.01 M Na₂SnO₃, 0.0005 M In(OH)₃, 0.0075 M ZnO as inhibitors serves as the electrolyte and the aluminum plate is selected as an anode for full cell tests. All air cathode electrodes consist of a gas diffusion layer, a current collector and a catalyst layer. Nickel foams or copper meshes are generally employed as current collectors due to excellent conductivity. The catalyst layers were prepared as follows: catalyst, active carbon, 60% polytetrafluoroethylene (PTFE) emulsion and acetylene black were uniformly mixed according to the mass ratio of 3:3:1 and then the mixture was rolled on a two-roll sheeter machine until the thickness was about 2 mm [7].

2.5. Density functional theory calculations

The theoretical calculations were conducted using the DMol³ software package in Materials Studio. The generalized gradient approximation (GGA) with Perdew-Burke-Ernzerhof (PBE) was applied. A periodic (4 × 4) supercell of graphene with FeN₄-coordinated configuration was built to study Fe-N-C. For Cu-Fe-N-C catalysts, CuN₃ structure is utilized to modify the optimized FeN₄ configuration. To evaluate the adsorption strength of O₂ on the model molecule catalysts, the adsorption energy of O₂ was calculated according to $E_{\text{ads}} = E_{\text{total}} - E_{\text{catalyst}} - E_{\text{adsorbate}}$, where *E_{catalyst}* and *E_{adsorbate}* represent the energy of the bare catalyst and the free oxygen molecule in the gas phase, respectively, *E_{total}* is the total energy of the catalysts with adsorbates.

The free energies of the ORR intermediates (*OOH, *O and *OH) absorbed on Fe-N-C and Cu-Fe-N-C configuration surface were calculated in accordance with ORR pathways proposed in literature [45–47]. The reaction Gibbs free energy of each ORR electron transfer steps for the standard four electron reaction pathway as described in the main text are related to the adsorption Gibbs free energies of the ORR intermediates [48]. The first electron transfer step can be expressed as:



The reaction Gibbs free energy for this step is expressed as:

$$\Delta G_1 = -2\Delta G_{H_2O} - \Delta G_{OOH} \quad (6)$$

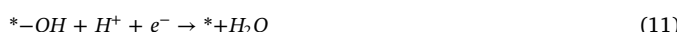
Herein, $\Delta G_{H_2O} = -2.46\text{eV}$ is the experimental formation energy of water molecule. Similarly, we have the following expressions for the rest of reaction steps:



$$\Delta G_2 = \Delta G_O - \Delta G_{OOH} \quad (8)$$



$$\Delta G_3 = \Delta G_{OH} - \Delta G_O \quad (10)$$



$$\Delta G_4 = -\Delta G_{OH} \quad (12)$$

3. Results and discussion

3.1. Structure and morphology characterization

In this work, a simple one-step pyrolysis method as illustrated in Fig. 1 was employed in the synthesis of Cu-Fe-N-C electrocatalysts. For comparison, Fe-N-C catalysts were also prepared in the same way without adding CuCl. The effect on ORR activity of Fe-N-C with various FeCl₂ contents was also studied (ESI, Fig. S1). The obtained Fe-N-C has the highest activity when the molar content of 1,10-phenanthroline is ten times than that of FeCl₂. As revealed by XRD patterns of Fe-N-C (ESI, Fig. S2), the obvious peak at 26.3° belongs to (002) plane of graphitic carbon, while the other diffraction peaks are characteristic of Fe₃C (JCPDS No.03-0411). SEM and TEM images in Fig. 2a–c demonstrate two different morphologies of carbon in Fe-N-C: porous nanosheets and bamboo-like carbon nanotubes. Meanwhile, some Fe-based nanoparticles are encapsulated in the surrounding nanosheets and nanotubes, forming a core-shell structure. The interplanar distance of 0.21 nm in Fig. 2d corresponds to the (211) plane of Fe₃C. Fe₃C nanoparticles are tightly wrapped in a graphitic carbon shell with a thickness of about 2 nm.

Cu-Fe-N-C samples with various Cu contents were prepared. As seen

from the LSV curves (ESI, Fig. S3), Cu-Fe-N-C electrocatalyst made from metal precursors with a 1:1 molar ratio of Fe to Cu shows the highest ORR catalytic activity. As expected, the sample with CuCl as the Cu source has a superior ORR activity than CuCl₂ as the precursor (ESI, Fig. S4), manifesting a functional model of CoO active site containing two redox sites, an iron heme and a distal copper [49].

Fig. 3a presents the XRD patterns of the Cu-Fe-N-C samples before and after acid leach. Compared with those of Fe-N-C, several additional peaks from Fe₂O₃ (JCPDS No.25-1402) and Cu (JCPDS No.65-9026) are observed for Cu-Fe-N-C. After acid leaching, the much weaker XRD peaks suggest that most of particles were removed. The BET surface area of Fe-N-C and Cu-Fe-N-C calculated from the N₂-adsorption isotherm in Fig. S5 (ESI) are 267.5 and 78.2 m² g⁻¹, respectively. The significant lower area in the latter could be ascribed to the synergic effect between the formation of larger diameter carbon nanotubes and the agglomeration of Fe₂O₃ and Cu nanoparticles during the pyrolysis after the introduction of copper sources [43]. For Cu-N-C without adding Fe sources, there are only three intensive characteristic peaks from Cu (JCPDS No.65-9026) in the XRD patterns (ESI, Fig. S6). From Fig. 2e, the intensities of these characteristic peaks become very weak after acid treatment, indicating that most of these nanoparticles could be removed. The morphology of Cu-Fe-N-C without acid treatment was analyzed by SEM and TEM. Comparing Fig. 3b with Fig. 1a, the diameter of carbon nanotubes in Cu-Fe-N-C is much larger. Besides the typical nanosheets and bamboo-like carbon nanotubes in Fe-N-C, worm-like carbon nanotubes with a diameter of 60~100 nm also exist in Cu-Fe-N-C (Fig. 3c–d). On the other hand, Cu-N-C sample consists of nanosheets with well-defined mesoporous feature (ESI, Fig. S7a–b). The formation of worm-like carbon nanotubes might be caused by the cooperative catalysis of Fe and Cu during pyrolysis. The HR-TEM image in Fig. 3e verify the existence of Fe₃C and graphitic carbon, but the thickness of the carbon layer increases to about 10 nm. A thicker carbon layer also results in reduction of BET surface area. The elemental mapping was performed to further investigate the elemental distribution in Cu-Fe-N-C in Fig. 3f. Fe (yellow) is intensively distributed in the interior of carbon nanotubes, while Cu (blue), N (green), O (purple) and C (red) are uniformly scattered on the whole surface. TEM and HR-TEM images of Cu-Fe-N-C after acid leaching (ESI, Fig. S8) reveal that the morphology and Fe₃C nanoparticles are well preserved. Because the bare Fe₃C nanoparticles would be dissolved in acid system, only those

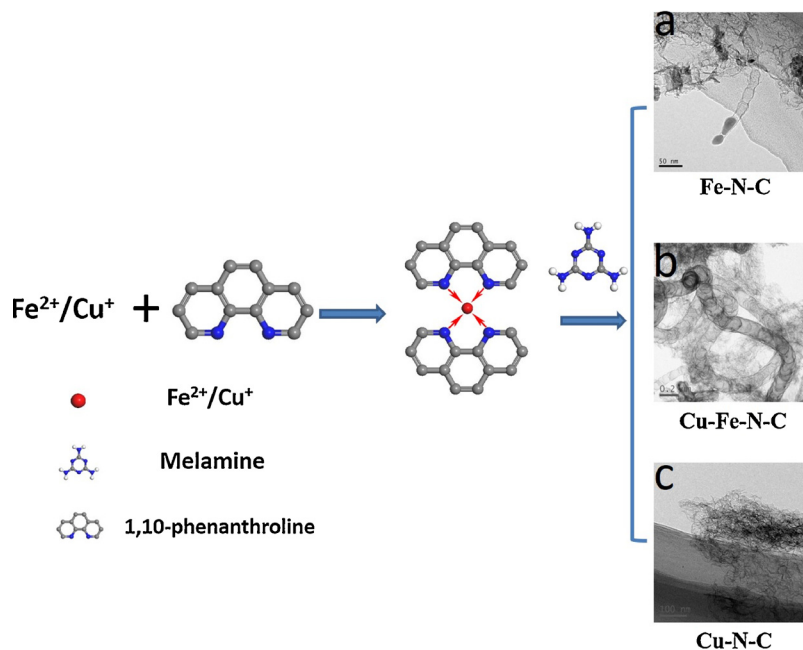


Fig. 1. Illustration of the synthesis procedure for Fe-N-C without adding Cu⁺ (a), Cu-Fe-N-C with both Fe²⁺ and Cu⁺ (b) and Cu-N-C without Fe²⁺ (c).

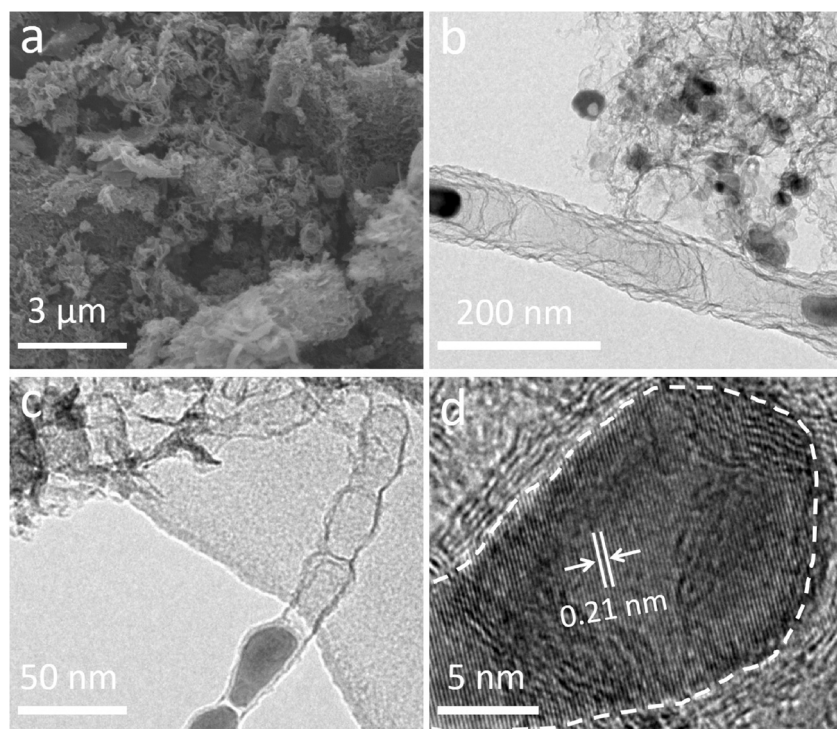


Fig. 2. (a) SEM, (b–c) TEM and (d) HR-TEM images of the resultant Fe-N-C sample.

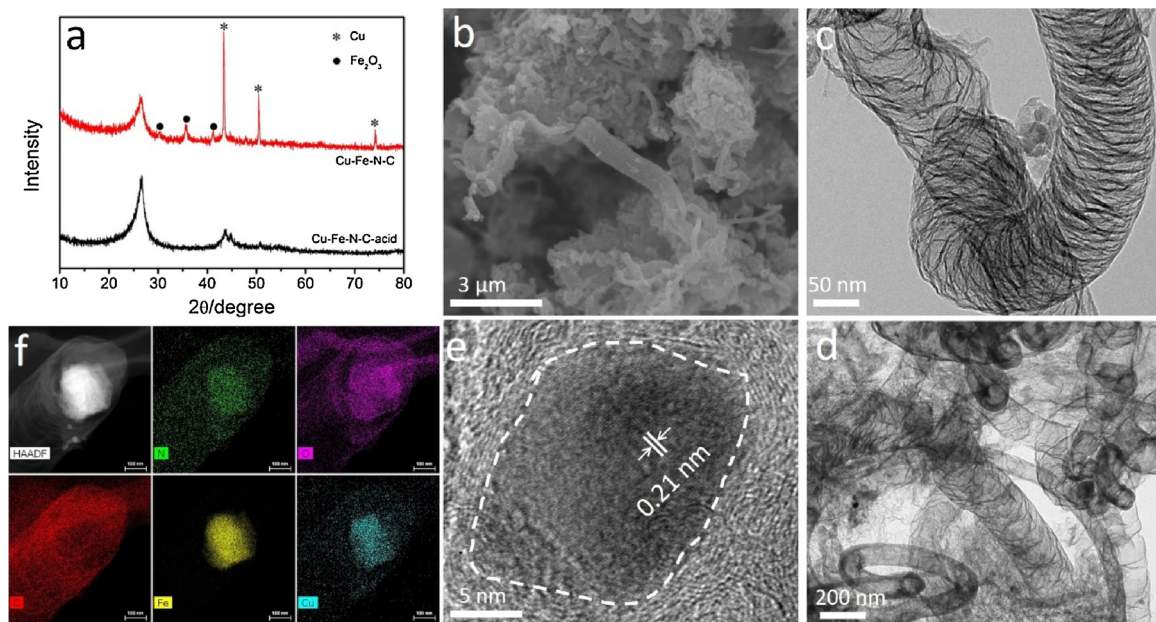


Fig. 3. (a) XRD patterns of the resultant Cu-Fe-N-C before (red) and after (black) acid leach, (b) SEM, (c–d) TEM, (e) HR-TEM images and (f) HAADF-STEM and elemental mapping images of Cu-Fe-N-C without acid treatment. (For interpretation of the references to colour in this figure legend, the reader is referred to the web version of this article).

encased by carbon layers could survive during the leaching process.

X-ray photoelectron spectroscopy (XPS) analysis was characterized to explore chemical composition and element valence states (Fig. 4). It is evident that the contents of Fe and Cu in the Cu-Fe-N-C are reduced after acid leaching from Fig. S9 and Table S1 (ESI). Moreover, the contents of metal and N in the Fe-N-C are higher than that of Cu-N-C, which is probably attributed to the higher coordination numbers of Fe (II) ion and 1,10-phenanthroline than that of Cu(I) ion. This is also confirmed by the total metal content and N content slightly decreased after copper substitution to equal molar iron in Fe-N-C. In the high-

resolution Fe2p spectrum of Fe-N-C in Fig. 4a, the main peaks at bonding energies of 710.6 eV and 723.8 eV are assigned to Fe(II) species [36,50,51]. After copper embedded in Fe-N-C, another pair peaks at 714.4 eV and 725.4 eV emerges (Fig. 4b), clearly indicating the surface-exposed Fe(II) and Fe(III) particles in Cu-Fe-N-C [36,51], while the characteristic peaks of Fe(III) (Fig. 2c) disappear after acid treatment. The Cu 2p curve of Cu-N-C apparently displays two peaks at 933.2 eV and 935.0 eV (Fig. 4d), corresponding to Cu(0) and Cu(II), respectively [52,53]. Cu(II) may be due to the oxidation of metallic Cu on the surface. The characteristic peak of Cu(II) in Cu-Fe-N-C was shifted

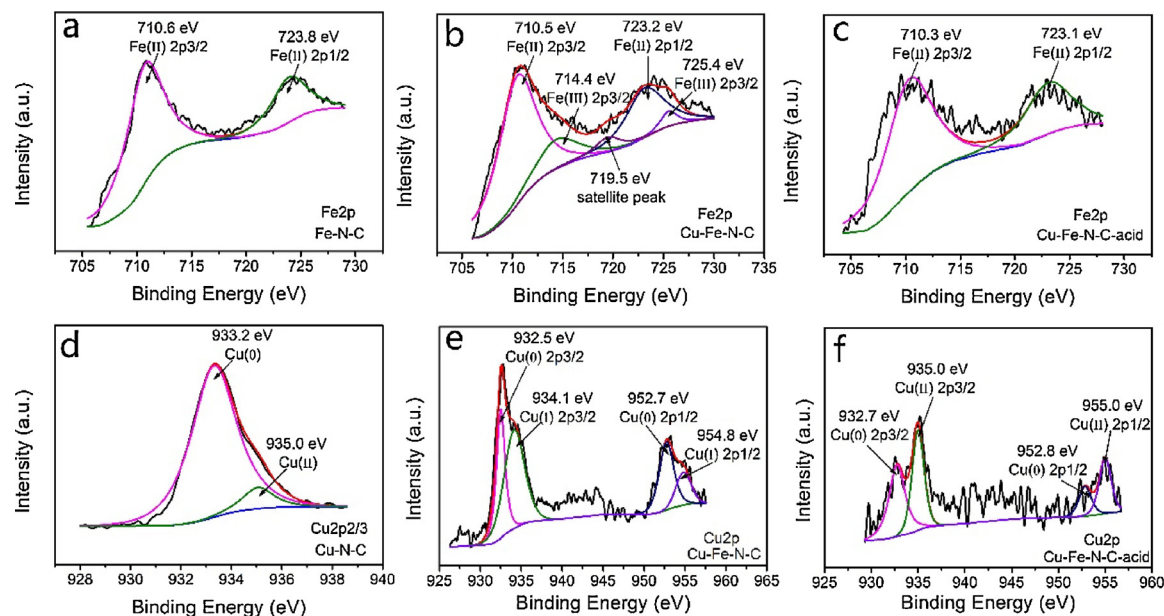


Fig. 4. The high-resolution Fe 2p XPS spectra of the Fe-N-C catalyst (a) and the Cu-Fe-N-C catalyst before (b) and after (c) acid treatment; Cu 2p XPS spectra of the Cu-N-C catalyst (d) and the Cu-Fe-N-C catalyst before (e) and after (f) acid treatment.

negatively to 934.7 eV (Fig. 4e), respectively. As more N atoms are coordinated with Fe(II) than Cu(I), the reduced N changed the electron density on Cu, thus resulting in less Cu(II) content than Cu-N-C [50]. In addition, the peak of Cu(I) turns up and Cu(0) was disappeared. From Fig. 4f, the content of Cu(I) was decreased after acid treatment, probably due to the conversion of Cu(I) to Cu(II) via the oxidation of Fe(III) in acid media. The N1s spectra of all samples (ESI, Fig. S9) are fitted into three different contributions of 398.6, 399.6 and 401.0 eV, in good agreement with the pyridinic, pyrrolic and graphitic N, respectively [13,15,54]. From Table S2, the content of graphitic N in the Cu-N-C is higher than that of Fe-N-C, which is probably attributed to the easier formation of graphitic N in the presence of Cu compared with Fe during the pyrolysis process. This is also confirmed by the graphitic N content slightly increased after copper substitution to equal molar iron in Fe-N-C. It should be pointed out that incorporation of copper results in increased content of graphitic N, suggesting that the existence of Cu can promote the formation of active graphitic N species [55,56]. Liao et al. [55] also reported that the XRD peak at 24° became sharper and shifted positively after Cu doping, indicating the increase of the graphitization degrees. In addition, the morphology of the catalysts changed dramatically, when Cu and Fe were added simultaneously. Particularly, when the molar ratio of Fe to Cu was adjusted to 1:1, the Fe-Cu-N/C exhibits a well-defined and uniform nanotube morphology, which could increase the graphitization degrees. It is noted that pyridinic and graphitic N generally act as the active sites for ORR [36]. That is, the incorporation of Cu boosts the interaction of between metal and N and increases the contents of active site on the surface of catalyst, contributing to the improved performance.

3.2. Electrocatalytic performance

To evaluate the ORR catalytic activity of these catalysts, we performed CV curves in Ar- and O₂-saturated 0.1 M KOH solutions, respectively. In Fig. S11 (ESI), Cu-Fe-N-C possesses a remarkable ORR peak at 0.873 V (vs RHE) in an O₂-saturated electrolyte. There are a couple of reversible redox peaks at about 0.64 V under O₂ and Ar, which could be due to the reduction/oxidation of Fe(III)/Fe(II) and/or Cu(I)/Cu(0) on the catalysts [57–59]. In addition, there is a characteristic peak around 0.87 V in O₂- and Ar-saturated electrolytes, assigned to the oxidation peaks of Cu(I) [59]. The excellent ORR activity

of Cu-Fe-N-C was also manifested by polarization curves. Cu-N-C, Fe-N-C and Pt/C were also conducted for comparison. LSV curves in Fig. 5a demonstrate that Cu-N-C has the lowest activity, as reflected by a low half-wave potential ($E_{1/2}$) of 0.78 V. Fe-N-C exhibits excellent performance with a $E_{1/2}$ of 0.84 V, even outperforming Pt/C catalyst ($E_{1/2} = 0.82$ V). The half-wave potential is further improved by 25 mV by introducing Cu in Fe-N-C (Fig. 5b) even with a much lower BET surface area. It should be noted that the BET surface area of Cu-Fe-N-C is much less than that of Fe-N-C, suggesting the significantly decreased numbers of active sites. This result also implies that the intrinsic catalytic activity of active sites in Cu-Fe-N-C should be much higher than those in Fe-N-C, suggesting an apparent synergistic effect between Fe- and Cu-modified carbon materials on ORR performance of catalysts. The ORR catalytic activity of Cu-Fe-N-C-acid was also performed under the same conditions (ESI, Fig. S12). The ORR catalytic activity of Cu-Fe-N-C after acid treatment slightly decreased in terms of half-wave potential and limiting-current density, indicating that the Fe₂O₃ and Cu nanoparticles in Cu-Fe-N-C are good for the ORR process to some extent.

To gain more details on ORR performance of Cu-Fe-N-C, the LSV curves at different rotating speeds from 400 to 1600 rpm were tested (Fig. 5c) and the electron-transferred number was calculated on the basis of Koutecky-Levich (K-L) plots (Fig. 5d). Note that the current density has a sudden change at the potential of 0.82 V with the rotating speed decreasing, which may be ascribed to the rapid depletion of oxygen during the full integration between catalyst and oxygen [7,60]. K-L plots in Fig. 5d reveals an electron transfer number of ~4, meaning that Cu-Fe-N-C catalyzed a 4-electron ORR between 0.50 V and 0.70 V in alkaline medium. The excellent catalytic activity was further verified by the much smaller Tafel slope (Fig. 5e) of 100.1 mV per decade at potential of 0.83–0.90 V, a little lower than that of Pt/C (100.3 mV per decade) and much smaller than that of Fe-N-C (103.1 mV per decade), revealing that the transfer of the first electron is the rate-determining step under Temkin conditions for the adsorption of intermediates [50,51]. The smaller Tafel slope of Cu-Fe-N-C than Pt/C suggests that the incorporation of Cu could restrain the overpotential increase at high current density, generating better ORR activity of Cu-Fe-N-C [51]. In other words, this result also implies that the similar ORR mechanisms for Cu-Fe-N-C and Pt/C in alkaline solution.

To further study the transferred electron number and production of PROS in the whole potential window (0~1.0 V), RRDE measurements

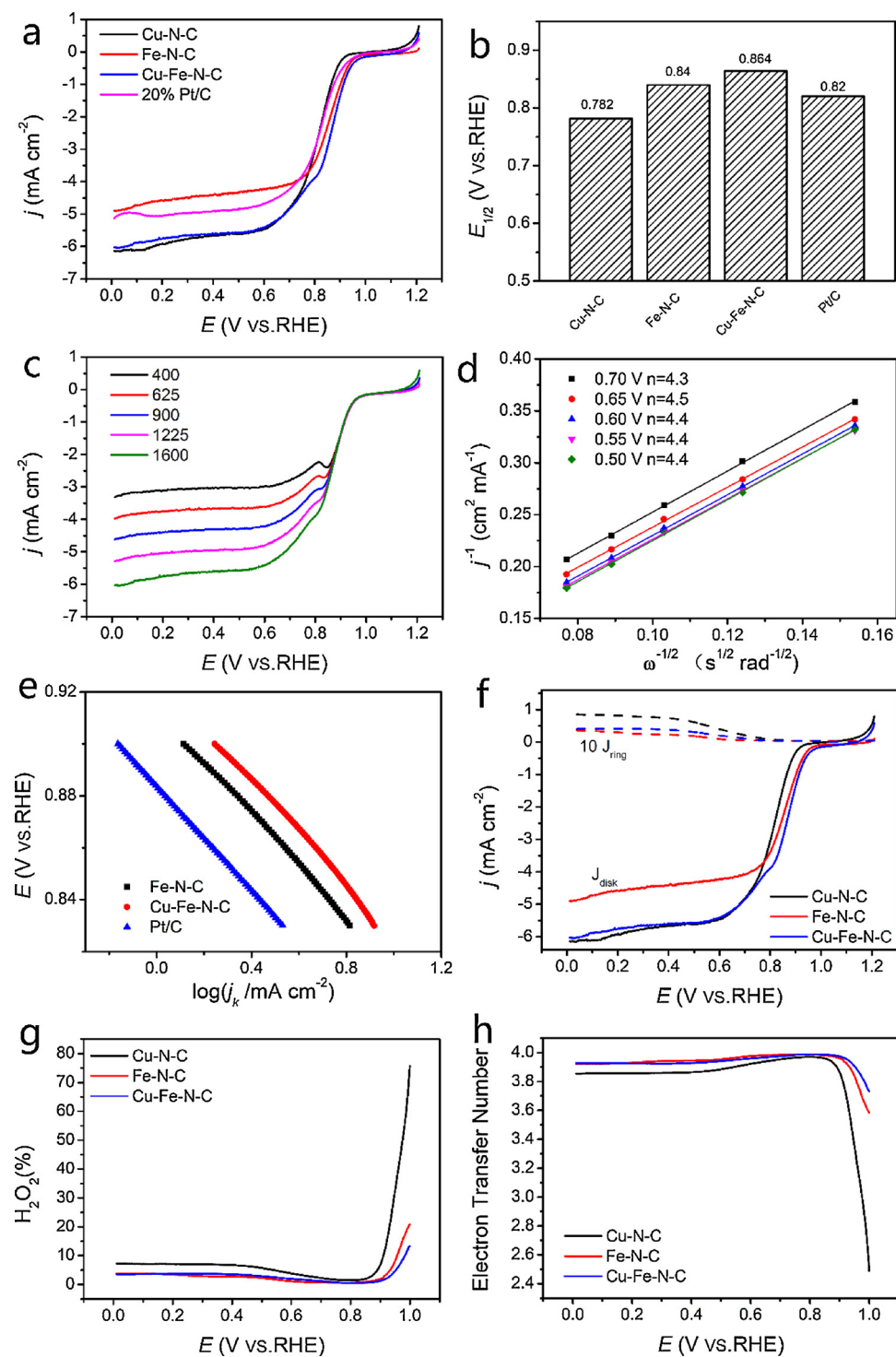


Fig. 5. (a) LSV curves of the Cu-Fe-N-C, Fe-N-C, Cu-N-C and Pt/C catalysts in O_2 -saturated 0.1 M KOH at 10 mV s^{-1} and 1600 rpm. (b) Half-wave potentials ($E_{1/2}$) of these catalysts. (c) LSV curves of Cu-FeN-C at different rotation rates. (d) Koutecky-Levich (K-L) plots for Cu-Fe-N-C at different potentials. (e) Tafel plots for the Cu-Fe-N-C, Fe-N-C and Pt/C catalysts. (f) RRDE voltammograms, (g) peroxide yield ($\text{H}_2\text{O}_2\%$) and (h) transferred electron number (n) for the Cu-Fe-N-C, Fe-N-C and Cu-N-C catalysts in O_2 -saturated 0.1 M KOH at 10 mV s^{-1} and 1600 rpm. The mass loading of catalysts was 0.243 mg cm^{-2} .

were performed (Fig. 5f). Obviously, Cu-Fe-N-C and Fe-N-C have much smaller ring current density than Cu-N-C. The peroxide yield and transferred electron number are calculated according to RRDE test results. Both Cu-Fe-N-C and Fe-N-C have lower peroxide percentage ($< 5\%$) and higher transferred electron number (~4) in the low potential ($0.20 \sim 0.90 \text{ V}$), while the former has much higher transferred electron number in the high potential (over 0.90 V), providing the evidence that the incorporation of copper can definitely promote the

ORR catalytic activity of Fe-N-C by reducing the overpotential and production of peroxide [61–64].

Fig. 6 presents the stability test of Cu-Fe-N-C and Pt/C by comparing the LSV curves before and after 2000 cycles between 1.2 and 0.6 V at 200 mV s^{-1} in O_2 -saturated 0.1 M KOH. Obviously, both catalysts display a negative shift in half-wave potential and decrease in limiting-current density. Moreover, such changes are distinctly different. In Fig. 6, Cu-Fe-N-C exhibits a very little negative shift for $E_{1/2}$ and 5%

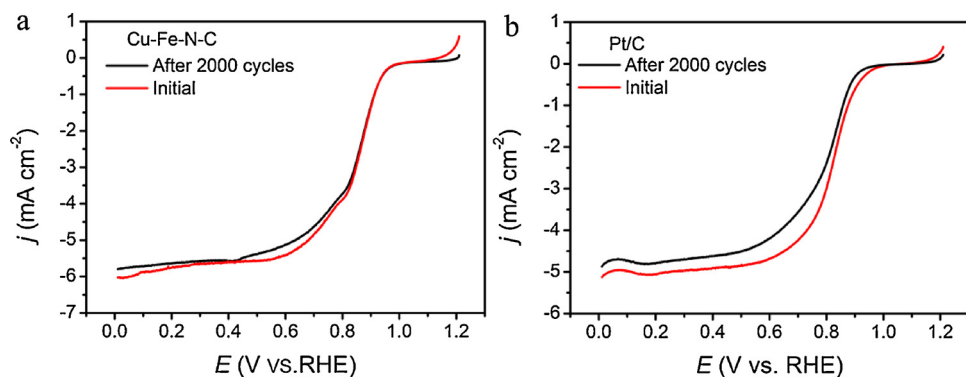


Fig. 6. Endurance test of the Cu-Fe-N-C (a) and Pt/C (b) catalysts for 2000 cycles at 200 mV s^{-1} in O_2 -saturated 0.1 M KOH .

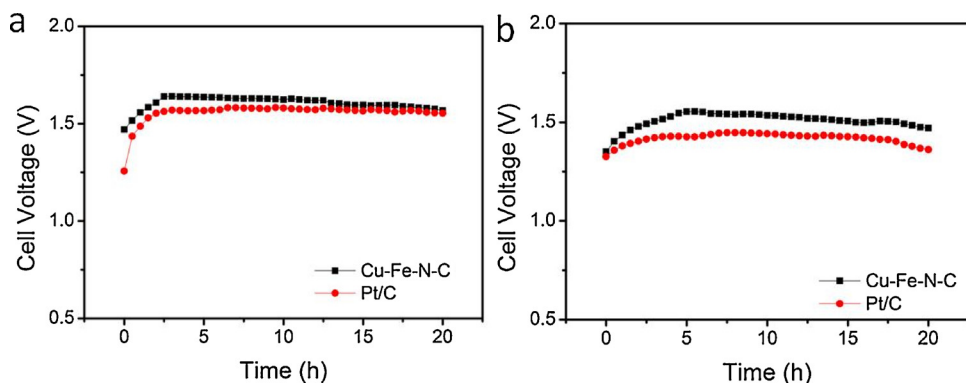


Fig. 7. The discharging curves for Al-air battery with Cu-Fe-N-C and Pt/C as cathode catalysts at constant current of 20 (a) and 40 (b) mA cm^{-2} .

decrease in limiting-current density, with a 35 mV shift ($E_{1/2}$) and 13.8% decrease for Pt/C. All results suggest that Cu-Fe-N-C possesses superior stability to Pt/C.

The practical catalytic performance of Cu-Fe-N-C as the cathode catalyst was evaluated in home-made Al-air battery and Pt/C was also tested under the same conditions as a reference. Fig. 7 demonstrates the discharging curves for Al-air batteries at 20 and 40 mA cm^{-2} , respectively. From Fig. 7a, the battery with Cu-Fe-N-C shows excellent performance with a maximum cell voltage (E_{\max}) of 1.64 V, which is comparatively higher than that of Pt/C (1.58 V) at 20 mA cm^{-2} . When discharged at 40 mA cm^{-2} (Fig. 7b), Cu-Fe-N-C exhibits much higher cell voltage than Pt/C. Moreover, the voltage degradation of Cu-Fe-N-C at 40 mA cm^{-2} for 20 h is 5%, while that using Pt/C catalyst reaches up to 7%. Moreover, the Al-air batteries with the Cu-Fe-N-C hybrid as the air cathode catalysts are used to power four different color LEDs and the results are shown in Fig. S13. Obviously, four different color LEDs lights are powered by two Al-air batteries in series. Note that the rated voltages of red and yellow are 2.1 V and those for blue and green are 3.4 V.

Taking account of the ORR catalytic activity order, Cu-N-C with metallic Cu nanoparticles and nanosheets morphology possesses the poorest activity, while Fe-N-C with Fe-based nanoparticles and the morphology of nanosheets and bamboo-like carbon nanotubes shows much better catalytic activity than Cu-N-C. Compared with Cu-N-C and Fe-N-C, Cu-Fe-N-C with metallic Cu and Fe-based nanoparticles and additional morphology of worm-like carbon nanotubes exhibits the best ORR catalytic activity. Note that Cu-Fe-N-C has much lower BET surface area than Fe-N-C, it comes to a conclusion that the incorporation of copper can catalyze the formation of worm-like carbon nanotubes and promote the ORR process. To further confirm the active sites for catalyzing ORR, Cu-Fe-N-C was leached in $0.5 \text{ M H}_2\text{SO}_4$ to remove Fe_2O_3 and Cu nanoparticles. XRD and XPS results confirm that most of these nanoparticles are removed and TEM image shows that some Fe_3C nanoparticles are kept during the acid treatment. Hence, Cu-Fe-N-C-acid exhibits similar ORR catalytic activity to Cu-Fe-N-C, revealing the

limited performance of metallic Cu and Fe_2O_3 nanoparticles towards ORR in Cu-Fe-N-C. In brief, the introduction of Cu makes a notable contribution to catalyzing ORR process in the form of $\text{Cu}_x\text{Fe}_y\text{N}_z\text{C}$.

To further identify the role of copper on the ORR activity in Cu-Fe-N-C, density functional theory (DFT) calculations utilizing the Dmol³ package have been conducted. Firstly, we calculate the adsorption energy of possible ORR species O_2 absorbed on the $\text{Fe}-\text{N}_4$ active sites. As seen from Fig. 8a, the active site of our synthesized Fe-N-C was modeled with a 32-atom graphene super cell with periodic boundary conditions in three dimensions, of which the lattice parameters are $a = 9.84 \text{ \AA}$ and $b = 8.52 \text{ \AA}$. The calculated adsorption energy on FeN_4 is -1.01 eV , consistent with the reported results [65,66]. Based on the optimum FeN_4 configuration (Fig. 8a), we mimic the coordination environments of CcO to model the active site of Cu-Fe-N-C. Meanwhile, we assume that Cu(I) coordinates with three N atoms [37,67,68]. To further characterize the effect of atomic distance from Fe to Cu on ORR performance, two types of CuN_3FeN_4 configurations were designed: Cu atom is adjacent to Fe in FeN_4 ($\text{CuN}_3\text{FeN}_4\text{-1}$, Fig. 8b) and a N atom is between Cu and Fe ($\text{CuN}_3\text{FeN}_4\text{-2}$, Fig. 8c). The binding energies of O_2 on Cu-modified FeN_4 configurations are -2.44 and -2.38 eV (Fig. 8b and c), respectively, much lower than that of FeN_4 . Hence, the additional Cu (I) species promotes the ORR activity of FeN_4 configuration by favoring the adsorption of O_2 . Comparing the binding energy of O_2 in Fig. 8b and c, the former is more conducive to the occurrence of oxygen reduction reaction.

To further manifest the important role of Cu in Cu-Fe-N-C catalyst, we calculate the free energy change according to the pathways of ORR in Eqs. (13)–(15) ($\text{H}_2\text{O(g)}$ and $\text{H}_2\text{(g)}$ are used for references) [45–47].



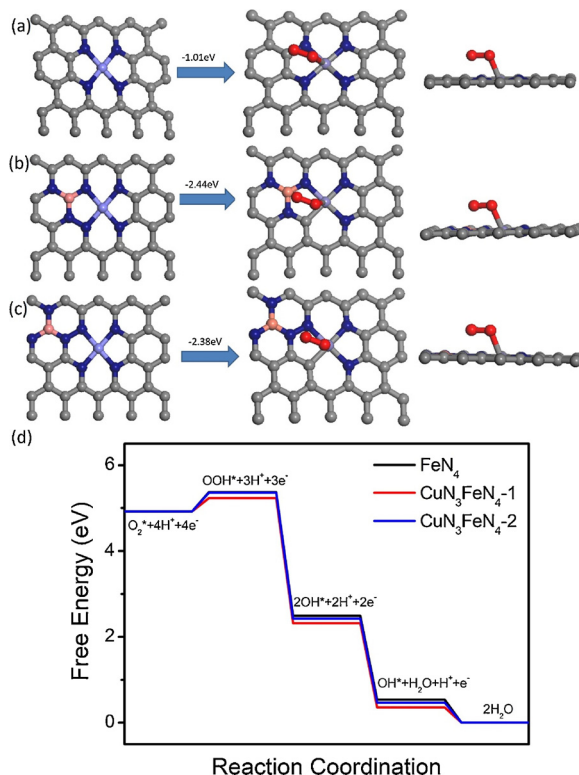


Fig. 8. Atomic model of FeN_4 (a), $\text{CuN}_3\text{FeN}_4\text{-}1$ (b) and $\text{CuN}_3\text{FeN}_4\text{-}2$ (c) cluster embedded in monolayer graphene (left) and optimized structure (right) of O_2 adsorbed on FeN_4 (a), $\text{CuN}_3\text{FeN}_4\text{-}1$ (b) and $\text{CuN}_3\text{FeN}_4\text{-}2$ (c) configurations. The calculated absorption of O_2 energy on FeN_4 (a), $\text{CuN}_3\text{FeN}_4\text{-}1$ (b) and $\text{CuN}_3\text{FeN}_4\text{-}2$ (c) configurations are shown above the blue arrows. Gray, blue, red, orange and wathet spheres stand for C, N, O, Cu and Fe atoms. (d) Free energy diagram of ORR on FeN_4 (a), $\text{CuN}_3\text{FeN}_4\text{-}1$ (b) and $\text{CuN}_3\text{FeN}_4\text{-}2$ (c) configurations. (For interpretation of the references to colour in this figure legend, the reader is referred to the web version of this article).



where the left superscript * represents an active site of FeN_4 and CuN_3FeN_4 configurations and $*\text{OOH}$, $*\text{O}$ and $*\text{OH}$ represent the absorbed ORR species.

Fig. 8d demonstrates the free energy diagram of every step for ORR intermediates adsorbed on FeN_4 , $\text{CuN}_3\text{FeN}_4\text{-}1$ and $\text{CuN}_3\text{FeN}_4\text{-}2$ configurations. It is obvious that all reaction steps on FeN_4 configuration are thermodynamically downhill except for the first step, which is 0.45 eV uphill. Hence, this step is considered as the rate-determining step of the whole ORR process. After the introduction of Cu, the trend is similar to that of FeN_4 , while the free energies of each step turn to be more negative. This result further states that Fe-N-C by partial copper substitution to iron could boost oxygen reduction activity. Comparing $\text{CuN}_3\text{FeN}_4\text{-}1$ with $\text{CuN}_3\text{FeN}_4\text{-}2$, we find that $\text{CuN}_3\text{FeN}_4\text{-}1$ has more negative free energy change of each step. That is, $\text{CuN}_3\text{FeN}_4\text{-}1$ is more beneficial to catalyzing the ORR process. It is deduced that the distance of Cu-Fe in the former (0.24 nm, the latter is 0.45 nm) is more close to that in CcO (0.28 nm) [69]. This can also explain why the introduction of copper could enhance ORR catalytic activity for Cu-Fe-N-C.

4. Conclusions

Summarily, inspired by CcO , we have successfully fabricated a highly efficient Cu-Fe-N-C hybrid for ORR through facile calcination of inorganic copper and iron chlorides together with 1,10-phenanthroline and melamine. It was found that copper partial substitution to iron could significantly improve the electrocatalytic activity of Fe-N-C and the content and types of added inorganic copper sources greatly

influenced the electrochemical activity. The half-wave potential of Cu-Fe-N-C reached 0.864 V, a 25 mV positive shift compared with Fe-N-C. Moreover, it also displayed better stability than Pt/C. In Al-air battery, Cu-Fe-N-C also demonstrated enhanced performance compared with Fe-N-C, highlighting the strong synergistic interactions between Cu and Fe species. DFT calculations further confirmed that the introduction of copper greatly improved the absorption of O_2 species, thus facilitating the occurrence of ORR. This work may offer new insights into developing novel ORR electrocatalysts based on bimetallic doping strategy.

Acknowledgements

This work was financially supported by the National Nature Science Foundation of China (No. 21571189 and No. 21671200), the Hunan Provincial Science and Technology Plan Project, China (No. 2016TP1007 and 2017TP1001), Innovation-Driven Project of Central South University (No. 2016CXS009), and High Performance Computing Center of CSU, China. The work at the Hong Kong University of Science and Technology was supported by Guangdong Special Fund for Science and Technology Development (Hong Kong Technology Cooperation Funding Scheme (201604030012, 201704030019, and 201704030065).

Appendix A. Supplementary data

Supplementary material related to this article can be found, in the online version, at doi:<https://doi.org/10.1016/j.apcatb.2018.09.044>.

References

- [1] M. Shao, Q. Chang, J.-P. Dodelet, R. Chenitz, Chem. Rev. 116 (2016) 3594–3657.
- [2] M. Lefèvre, E. Proietti, F. Jaouen, J.-P. Dodelet, Science 324 (2009) 71–74.
- [3] E. Antolini, Appl. Catal. B: Environ. 88 (2009) 1–24.
- [4] M. Prabu, K. Ketpang, S. Shammugam, Nanoscale 6 (2014) 3173–3181.
- [5] X. Ge, Y. Liu, F.W. Goh, T.S. Hor, Y. Zong, P. Xiao, Z. Zhang, S.H. Lim, B. Li, X. Wang, Z. Liu, ACS Appl. Mater. Interfaces 6 (2014) 12684–12691.
- [6] Y. Tang, L. Lu, H.W. Roesky, L. Wang, B. Huang, J. Power Sources 138 (2004) 313–318.
- [7] J. Li, Z. Zhou, K. Liu, F. Li, Z. Peng, Y. Tang, H. Wang, J. Power Sources 343 (2017) 30–38.
- [8] B. Robert, Ind. Robot: Int. J. 42 (2015) 186–191.
- [9] M. Shao, A. Peles, K. Shoemaker, Nano Lett. 11 (2011) 3714–3719.
- [10] Y. Hou, T. Huang, Z. Wen, S. Mao, S. Cui, J. Chen, Adv. Energy Mater. 4 (2014) 1400337.
- [11] Q.C. Tran, V.-D. Dao, H.Y. Kim, K.-D. Jung, H.-S. Choi, Appl. Catal. B: Environ. 204 (2017) 365–373.
- [12] L. Dai, Acc. Chem. Res. 46 (2013) 31–42.
- [13] N. Daems, X. Sheng, I.F. Vankelecom, P.P. Pescarmona, J. Mater. Chem. A 2 (2014) 4085–4110.
- [14] W.J. Lee, U.N. Maiti, J.M. Lee, J. Lim, T.H. Han, S.O. Kim, Chem. Commun. 50 (2014) 6818–6830.
- [15] R. Liu, D. Wu, X. Feng, K. Mullen, Angew. Chem. Int. Ed. 49 (2010) 2565–2569.
- [16] H. Yu, L. Shang, T. Bian, R. Shi, G.I. Waterhouse, Y. Zhao, C. Zhou, L.Z. Wu, C.H. Tung, T. Zhang, Adv. Mater. 28 (2016) 5080–5086.
- [17] I.-A. Choi, D.-H. Kwak, S.-B. Han, J.-Y. Park, H.-S. Park, K.-B. Ma, D.-H. Kim, J.-E. Won, K.-W. Park, Appl. Catal. B: Environ. 211 (2017) 235–244.
- [18] M. Hamdani, R. Singh, P. Chartier, Int. J. Electrochem. Sci. 5 (2010) 556–577.
- [19] Y. Tang, H. Qiao, H. Wang, P. Tao, J. Mater. Chem. A 1 (2013) 12512–12518.
- [20] H. Zhang, H. Li, H. Wang, K. He, S. Wang, Y. Tang, J. Chen, J. Power Sources 280 (2015) 640–648.
- [21] H. Zhang, H. Qiao, H. Wang, N. Zhou, J. Chen, Y. Tang, J. Li, C. Huang, Nanoscale 6 (2014) 10235–10242.
- [22] J. Chen, N. Zhou, H. Wang, Z. Peng, H. Li, Y. Tang, K. Liu, Chem. Commun. 51 (2015) 10123–10126.
- [23] A. Gabe, J. García-Aguilar, Á. Berenguer-Murcia, E. Morallón, D. Cazorla-Amorós, Appl. Catal. B: Environ. 217 (2017) 303–312.
- [24] H. Zhang, W. Tian, L. Zhou, H. Sun, M. Tade, S. Wang, Appl. Catal. B: Environ. 223 (2018) 2–9.
- [25] R. Jasinski, Nature 201 (1964) 1212–1213.
- [26] S. Pan, Z. Cai, Y. Duan, L. Yang, B. Tang, B. Jing, Y. Dai, X. Xu, J. Zou, Appl. Catal. B: Environ. 219 (2017) 18–29.
- [27] W. Yang, X. Liu, X. Yue, J. Jia, S. Guo, J. Am. Chem. Soc. 137 (2015) 1436–1439.
- [28] W.J. Jiang, L. Gu, L. Li, Y. Zhang, X. Zhang, L.J. Zhang, J.Q. Wang, J.S. Hu, Z. Wei, L.J. Wan, J. Am. Chem. Soc. 138 (2016) 3570–3578.
- [29] Z.Y. Wu, X.X. Xu, B.C. Hu, H.W. Liang, Y. Lin, L.F. Chen, S.H. Yu, Angew. Chem. Int. Ed. 127 (2015) 8297–8301.

- [30] J. Li, N. Zhou, J. Song, L. Fu, J. Yan, Y. Tang, H. Wang, ACS Sustain. Chem. Eng. 6 (2017) 413–421.
- [31] S. Cai, Z. Meng, H. Tang, Y. Wang, P. Tsiaikaras, Appl. Catal. B: Environ. 217 (2017) 477–484.
- [32] D.-H. Kwak, S.-B. Han, Y.-W. Lee, H.-S. Park, I.-A. Choi, K.-B. Ma, M.-C. Kim, S.-J. Kim, D.-H. Kim, J.-I. Sohn, K.-W. Park, Appl. Catal. B: Environ. 203 (2017) 889–898.
- [33] J. Li, J. Chen, H. Wang, Y. Ren, K. Liu, Y. Tang, M. Shao, Energy Storage Mater. 8 (2017) 49–58.
- [34] J.S. Li, S.L. Li, Y.J. Tang, M. Han, Z.H. Dai, J.C. Bao, Y.Q. Lan, Chem. Commun. 51 (2015) 2710–2713.
- [35] S. Li, Y. Hu, Q. Xu, J. Sun, B. Hou, Y. Zhang, J. Power Sources 213 (2012) 265–269.
- [36] L. Lin, Q. Zhu, A.W. Xu, J. Am. Chem. Soc. 136 (2014) 11027–11033.
- [37] N.K.D. James, P. Collman, Richard A. Decréau, Ying Yang, Yi-Long Yan, T.A.E. Wataru Ebina, Christopher E.D. Chidsey, Science 315 (2007) 1565–1568.
- [38] M. Jahan, Z. Liu, K.P. Loh, Adv. Funct. Mater. 23 (2013) 5363–5372.
- [39] R.P. Liang, X.Y. Meng, C.M. Liu, J.D. Qiu, Electrophoresis 32 (2011) 3331–3340.
- [40] B. Luo, X. Li, J. Yang, X. Li, L. Xue, X. Li, J. Gu, M. Wang, L. Jiang, Anal. Methods 6 (2014) 1114.
- [41] K. Maeda, K. Teramura, D. Lu, T. Takata, N. Saito, Y. Inoue, K. Domen, Nature 440 (2006) 295–295.
- [42] Q. He, X. Yang, X. Ren, B.E. Koel, N. Ramaswamy, S. Mukerjee, R. Kostecki, J. Power Sources 196 (2011) 7404–7410.
- [43] M. Kato, T. Murotani, I. Yagi, Chem. Lett. 45 (2016) 1213–1215.
- [44] Y. Meng, W. Song, H. Huang, Z. Ren, S.Y. Chen, S.L. Suib, J. Am. Chem. Soc. 136 (2014) 11452–11464.
- [45] J.R.J.K. Nørskov, A. Logadottir, L. Lindqvist, J. Phys. Chem. B 108 (2004) 17886–17892.
- [46] H. Kim, K. Lee, S.I. Woo, Y. Jung, Phys. Chem. Chem. Phys. 13 (2011) 17505–17510.
- [47] L. Yu, X. Pan, X. Cao, P. Hu, X. Bao, J. Catal. 282 (2011) 183–190.
- [48] J.K. Nørskov, J. Rossmeisl, A. Logadottir, et al., J. Phys. Chem. B 108 (46) (2004) 17886–17892.
- [49] N.K.D. James, P. Collman, Richard A. Decréau, Ying Yang, Yi-Long Yan, Wataru Ebina, Todd A. Eberspacher, Christopher E.D. Chidsey, Science 315 (2007) 1565–1568.
- [50] R. Cao, R. Thapa, H. Kim, X. Xu, M. Gyu Kim, Q. Li, N. Park, M. Liu, J. Cho, Nat. Commun. 4 (2013) 2076.
- [51] J. Liu, X. Sun, P. Song, Y. Zhang, W. Xing, W. Xu, Adv. Mater. 25 (2013) 6879–6883.
- [52] H. Wu, H. Li, X. Zhao, Q. Liu, J. Wang, J. Xiao, S. Xie, R. Si, F. Yang, S. Miao, X. Guo, G. Wang, X. Bao, Energy Environ. Sci. 9 (2016) 3736–3745.
- [53] H. Yu, A. Fisher, D. Cheng, D. Cao, ACS Appl. Mater. Interfaces 8 (2016) 21431–21439.
- [54] J. Song, T. Xu, M.L. Gordin, P. Zhu, D. Lv, Y.-B. Jiang, Y. Chen, Y. Duan, D. Wang, Adv. Funct. Mater. 24 (2014) 1243–1250.
- [55] M. Kuang, Q. Wang, P. Han, G. Zheng, Adv. Energy Mater. 7 (2017) 1700193.
- [56] W. Fan, Z. Li, C. You, X. Zong, X. Tian, S. Miao, T. Shu, C. Li, S. Liao, Nano Energy 37 (2017) 187–194.
- [57] Y. Zhu, B. Zhang, X. Liu, D.W. Wang, D.S. Su, Angew. Chem. Int. Ed. 53 (2014) 10673–10677.
- [58] H.-H. Li, C.-H. Cui, S. Zhao, H.-B. Yao, M.-R. Gao, F.-J. Fan, S.-H. Yu, Adv. Energy Mater. 2 (2012) 1182–1187.
- [59] M.R. Zamanzad Ghavidel, A.H.A. Monteverde Videla, S. Specchia, E.B. Easton, Electrochim. Acta 230 (2017) 58–72.
- [60] Y. Wang, A. Kong, X. Chen, Q. Lin, P. Feng, ACS Catal. 5 (2015) 3887–3893.
- [61] D. Deng, L. Yu, X. Chen, G. Wang, L. Jin, X. Pan, J. Deng, G. Sun, X. Bao, Angew. Chem. Int. Ed. 52 (2013) 371–375.
- [62] Y. Hu, J.O. Jensen, W. Zhang, L.N. Cleemann, W. Xing, N.J. Bjerrum, Q. Li, Angew. Chem. Int. Ed. 53 (2014) 3675–3679.
- [63] D. Huang, Y. Luo, S. Li, B. Zhang, Y. Shen, M. Wang, Nano Res. 7 (2014) 1054–1064.
- [64] H.C. Huang, I. Shown, S.T. Chang, H.C. Hsu, H.Y. Du, M.C. Kuo, K.T. Wong, S.F. Wang, C.H. Wang, L.C. Chen, Adv. Funct. Mater. 22 (2012) 3500–3508.
- [65] K. Liu, S. Kattel, V. Mao, G. Wang, J. Phys. Chem. C 120 (2016) 1586–1596.
- [66] J. Zhang, Z. Wang, Z. Zhu, J. Power Sources 255 (2014) 65–69.
- [67] Y. Ma, P.B. Balbuena, Chem. Phys. Lett. 440 (2007) 130–133.
- [68] P.B.B. Yixuan Wang, J. Phys. Chem. B 109 (2005) 18902–18906.
- [69] A.H. Tsukihara, E. Yamashita, et al., Science 269 (1995) 1069.